J Therm Spray Tech
https://doi.org/10.1007/s11666-022-01474-1

PEER REVIEWED

Evaluation of CMAS Resistance and Failure Behavior for Phase Composite Thermal Barrier Coatings

X. Ma[1] · **P. Ruggiero**[1] · **G. Wildridge**[2]

Submitted: 27 May 2022 / in revised form: 12 September 2022 / Accepted: 28 September 2022

Abstract Environmental degradation of thermal barrier coatings (TBCs) by molten deposits, which include calcium magnesium alumino-silicates (CMAS), is one of the vital factors that result in the failure of thermal barrier coatings. This problem has been exacerbated due to increases in turbine engine inlet temperatures as a means to accommodate the demand for higher fuel efficiency. A new phase composite ceramic had been developed and evaluated for the topcoat of a durable thermal barrier coating (TBC) system with low thermal conductivity properties and improved erosion resistance. The primary goal of this research is to continue exploring the behavior of CMAS resistance of the phase composite TBC at high temperatures. The effects of CMAS attack and thermal exposure on the TBC degradation were investigated in experimental runs. In addition, a YAG-modified layer over the top of the TBC was applied in an attempt to improve the CMAS resistance of the TBC system. The evaluation of CMAS resistance was focused on the most important characteristics of coating microstructure including CMAS penetration, test condition factors, and mode of failure. The mechanisms for the CMAS infiltration and the TBC damages were discussed based on the analyses of the CMAS corroded samples in detail.

Keywords CMAS · failure mechanism · low thermal conductivity · test and evaluation · thermal barrier coatings (TBCs) · YAG

Introduction

Recently, the increase in combustion chamber temperatures of gas turbine engines and their operation in particle (silicate sand, ash and dust)-contaminated environments leads to ingestion, adhesion and infiltration of molten calcia–magnesia–alumino–silicate (CMAS) in thermal barrier coatings (TBCs) on hot section components. The adhesive CMAS molten on TBC surfaces and its mitigation into the ceramic topcoat in TBCs could result in more severe coating degradation and early failure (Ref 1-3).

A typical zirconia-based 8YSZ-TBC system is particularly vulnerable to high temperature CMAS attack. The mechanisms of CMAS attack and damages had been investigated and identified (Ref 4-6). Generally, molten CMAS adheres to the TBC surfaces and penetrates into the TBC through cracks and pores in APS-TBCs and grain boundaries in EB-PVD TBCs. Subsequently, CMAS may cause deteriorious changes in the chemical and mechanical properties of the TBCs. Upon cooling and solidifying of the molten CMAS, the TBC layer becomes rigid. This change induces strain responsible for TBC cracking, delamination

---

This article is an invited paper selected from presentations at the 2022 International Thermal Spray Conference, held May 4-6, 2022 in Vienna, Austria, and has been expanded from the original presentation. The issue was organized by André McDonald, University of Alberta (Lead Editor); Yuk-Chiu Lau, General Electric Power; Fardad Azarmi, North Dakota State University; Filofteia-Laura Toma, Fraunhofer Institute for Material and Beam Technology; Heli Koivuluoto, Tampere University; Jan Cizek, Institute of Plasma Physics, Czech Academy of Sciences; Emine Bakan, Forschungszentrum Jülich GmbH; Šárka Houdková, University of West Bohemia; and Hua Li, Ningbo Institute of Materials Technology and Engineering, CAS.

✉ X. Ma
chin.ma@cwst.com

[1] Curtiss-Wright Surface Technologies, East Windsor, CT, USA

[2] IMR Test Labs, Lansing, NY, USA

and even spallation attributed to the thermal expansion mismatch between the TBC and CMAS. The TBC chemically modified by CMAS penetration and chemical reaction can also become unstable in its phase structure and further reduce its longevity. Chemical interactions that occur between the molten or semi-molten CMAS and TBC are quite complicated and depend on the chemical compositions, basicity, temperatures and coating structures (Ref 7).

Researchers have utilized many approaches to improve TBC CMAS resistance via modifying TBC chemistry (Ref 8-13). Common methods include: (1) Adding solute dopants, such as Al^{3+} and Ti^{4+}, to TBC to elicit the crystallization of penetrating CMAS glass front, subsequently arresting it and sequentially slowing down the CMAS migration inward; (2) Adding active oxides into TBC to capture the molten CAMS by promoting the interaction; (3) to change and inhibit interaction by some additives to alter the basicity of CMAS/TBC system; (4) to use zirconate material for topcoat.

In our previous work, a concept of phase composite ceramic had been proposed for the topcoat of a durable and low-k TBC system. This research showed promising performance-related benefits over conventional single-phase TBCs, including durability, material affordability, thermal stability and low thermal conductivity (Ref 14, 15), as shown in Fig. 1. The present work is to continue the effort to explore the TBC behaviors of CMAS attack at different test conditions. In addition, the attempt to further improve the TBC CMAS resistance was made by modifying the chemical composition of the top layer of the TBC. The investigation was focused on the macro surface, reaction layers and phase composition of all the tested samples. The characteristics of the resistance to CMAS corrosion of the low-k TBC and YAG (yttrium aluminum garnet: $Al_5O_{12}Y_3$) additive were studied and the related mechanisms were discussed.

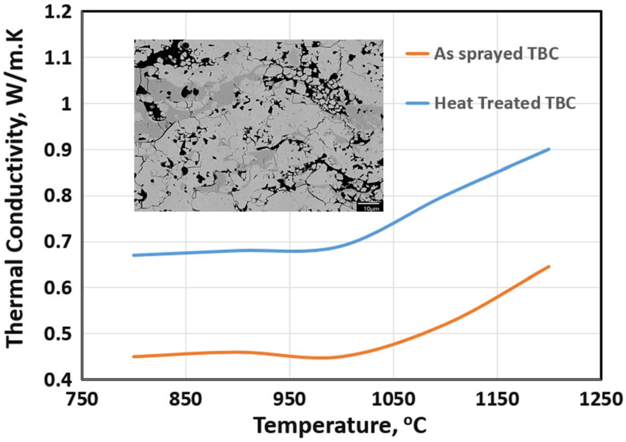

Fig. 1 Thermal conductivity data of as-sprayed and heat treated at 1300°C/25 h for a typical phase composite TBC

Experimental

Preparation of Coating Specimens

TBC specimens used in CMAS tests are listed in Table 1. The TBC samples were produced by Curtiss-Wright Surface Technologies ("CWST") using a F4 plasma torch (Metco, Westbury, NY) for ceramic topcoats and a Jet Kote-3000 HVOF torch (Stellite, Goshen, IN) for a metallic CoNiCrAlY bondcoat (CO-210-24, Praxair) onto Haynes 188 disk substrates (25 mm in diameter). A rough CoNiCrAlY flash layer over the dense alloy bondcoat was applied by the HVOF process to improve interface bonding between the bondcoat and the topcoat. An interlayer of t' phase zirconia was deposited over the bondcoat prior to applying the phase composite topcoat. For the sample #G3, a mixture of the low-k TBC (sample #G2) and yttrium aluminum garnet (YAG) was applied as a top layer, as shown in Fig. 2.

The optimal spray parameters were employed for fabricating the composite phase TBC. More details were disclosed in previous work (Ref 14). For comparison, regular 8YSZ TBC (Sample #G1) also were prepared. The TBC specimens have a typical porosity of 13 ~ 15% and a topcoat thickness of about 200 µm.

CMAS Attack Test

CMAS corrosion tests were performed by applying CMAS sands on the surfaces of the TBC samples demonstrated in Table 2. The CMAS sand was obtained from a commercial source (AFRL-02 test dust, PTI Inc., USA). AFRL-02 test dust was made from 34% Quartz, 30% Gypsum, 17% Aplite, 14% Dolomite and 5% Salt. DSC/DTA scans data showed that the CMAS sand has a melting temperature at 1150-1200°C (Ref 16). The sand was mixed with alcohol into a slurry, then brushed evenly on the surfaces of the TBC samples. The CMAS sand dosage on the surfaces were controlled at about 35 ± 2 mg/cm^2. For the TBC

Table 1 List of TBCs used for CMAS corrosion tests

Sample Code #	Main Chemicals for Topcoats
G1	ZrO_2-$8Y_2O_3$
G2	8YS/Two-phase (t' + c) low-k ZrO_2
G3	8YSZ/Low-k ZrO_2 + YAG

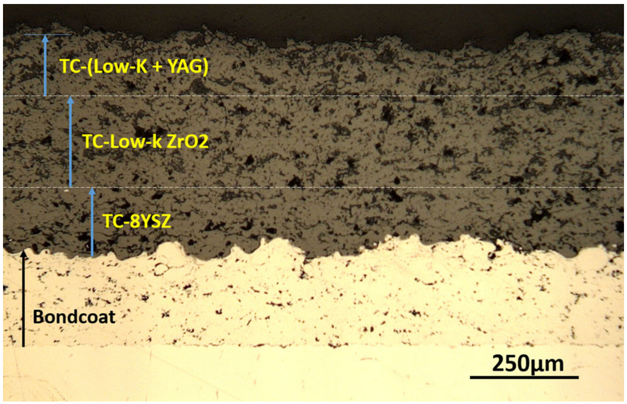

Fig. 2 Microstructure of a typical TBC sample #G3 with a modified top layer by adding YAG to the matrix of the composite phase TBC

Table 2 List of TBC samples for CMAS attack tests

Sample Code #	Test Samples and Duration (hrs)		
	TBC: G1	TBC: G2	TBC: G3
G1-5	5		
G2-5		5	
G3-5			5
G2-25-5, 15, 35		25	
G1-120	120		
G2-120		120	
G3-120			120

samples #G2-25-5, 15, 35, they have a CMAS dosage mass at 5, 15 and 35 mg/cm^2, respectively.

All the CMAS deposited TBC samples were tested in a box furnace in air isothermally at 1250 ± 25°C for different durations as given in Table 2. The test samples were placed inside the furnace, then heated to the isothermal temperature at a rate of about 50°C/min. After the tests were done, the furnace power was turned off and the samples remained inside until the furnace cooled down to room temperature.

Coating Characterization

The microstructures and material properties of TBC samples were evaluated and characterized using different technologies in as-sprayed and tested coating conditions. The coating microstructures on cross-sections and eroded surfaces were examined by optical microscope and SEM. The chemical compositions in selected samples and coating sections were analyzed by energy-dispersive-X-ray spectroscopy (EDXS) equipped with the SEM. The tested samples #G3-5 and #G3-120 were analyzed by SEM/EDXS method. In addition, the tested samples #G1, 2, 3-5 were examined by X-ray diffraction (XRD) method for phase identification, phase quantity and lattice parameter measurement. The XRD examination was carried out using a computer-controlled diffractometer (MiniFlex 600, Rigaku, Tokyo, Japan), with CuK-alpha 0.154 nm radiation.

Results and Discussion

Effect of CMAS Dosage on TBC Behavior

The TBC specimens #G2-25-5, 15, 35 were tested in air at 1250°C for 25 h, with the surface dosages of CMAS sand of 5, 15 and 35 mg/cm^2, respectively. Figure 3 shows the optical top views of three TBC samples #G2-25 (G2−5: 5 mg/cm^2; G2−15: 15 mg/cm^2; G2−35: 35 mg/cm^2) after the CMAS exposure. The damage of the CMAS existence to the TBC samples is obvious, and the degree of damage tends to become more severe with the increase of the CMAS dosage. The damage modes for those TBC samples are identified as surface buckling at 5 mg/cm^2 mass load, major cracking and local delamination or spallation within the ceramic layers at 15 mg/cm^2, and TBC catastrophic spallation at the bondcoat/topcoat interface at 35 mg/cm^2. The observation of the distribution of the molten CMAS adhered on the TBC surfaces indicates discontinuous coverage at low dosage of 5 mg/cm^2; locally concentrated coverage at a medium dosage of 15 mg/cm^2; and nearly complete coverage at the high dosage of 35 mg/cm^2.

The surface morphologies and the cross-section microstructures of the tested TBC samples are examined and the paths of CMAS infiltration into the coatings are schematically shown in Fig. 4. The CMAS infiltration process progresses in a sequence of (1) Wetting and spreading of molten CMAS on the TBC surfaces. The whole wetting process starts with a short-time spread-out stage and the long-time liquid-flow stage. Gu et al. found that the CMAS begins to melt and wet the surface of the samples at 1250°C, and the dynamic contact angle decreases dramatically with time during this spreading process. The wetting contact angles are in the range of 3 to 20°, depending on the substrates (Ref 16). In the thermal sprayed TBCs, the contact angles also should be associated with the surface morphologies including roughness, grain size defects, and so on. (2) When the spreading process reaches a steady-state, the CMAS infiltration process follows. It is believed that the infiltration starts from the locations of coating defects. In Fig. 4, several types of coating defects are indicated in the TBC topcoat. Crack type 1 is for the intrinsic coating cracks formed during the coating process, typically, in micro-size. Crack type 2 is for the cracking caused by the CMAS penetration and

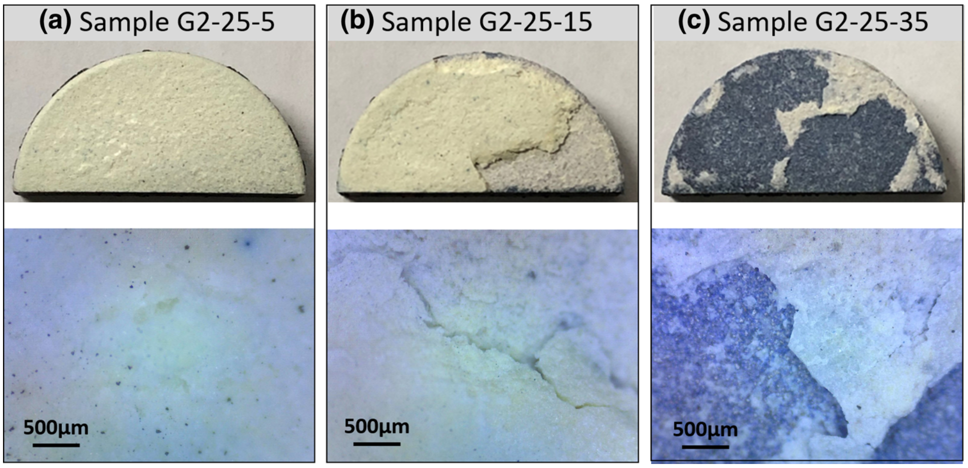

Fig. 3 Top views of the TBC samples after CMAS tests at 1250°C for 25 h, with different CMAS dosages. Sample A: G2-25-5, 5 mg/cm^2; Sample B: G2-25-15, 15 mg/cm^2; Sample C: G2-25-35, 35 mg/cm^2

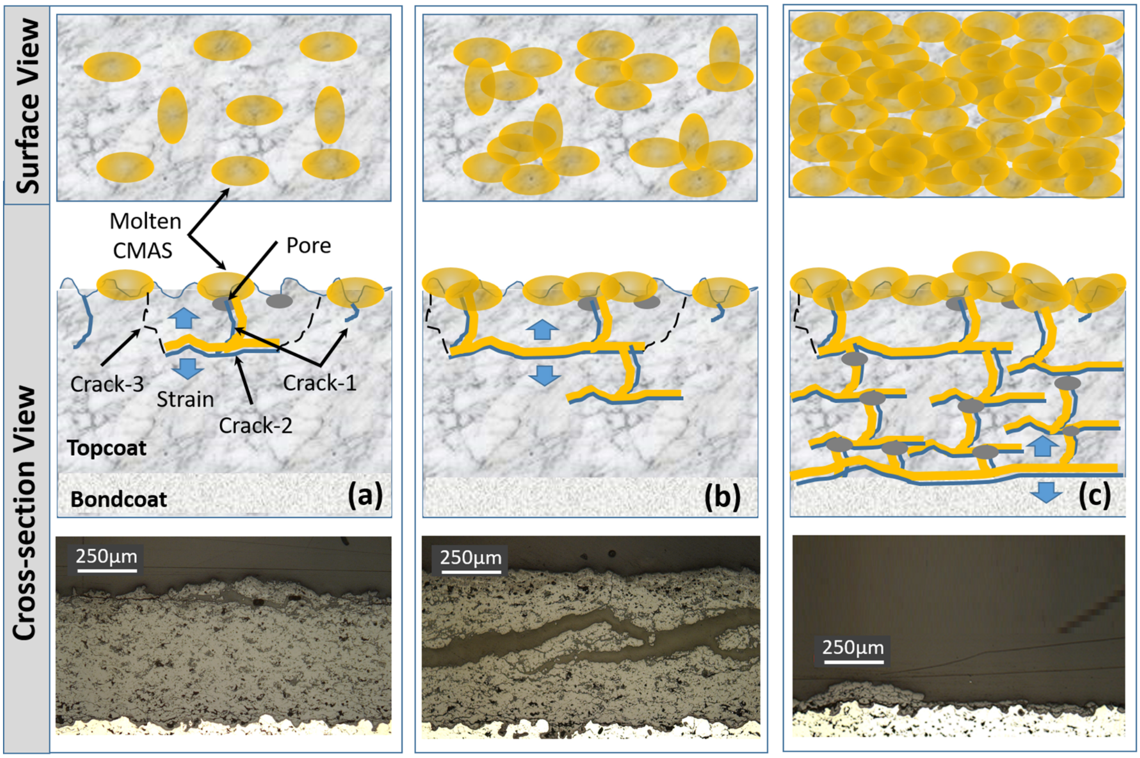

Fig. 4 Schematic of the effect of CMAS dosage on the damage mechanisms in the TBCs. (a) low dosage with local coverage; (b) medium dosage with high coverage; (c) high dosage with full coverage

associated strain, typically, in macro-size. Crack type 3 is for the cracking consequentially resulting from the cracking type 2 and will lead to coating delamination, spallation, and or buckling. Coating porosity in both micro and macro-sizes plays key roles as preferred start points for CMAS penetration. (3) When the molten CMAS enters the coating, it will continue to penetrate inward through the coating defects primarily macro-pores and widely open cracks.

The effects of CMAS dosage on the penetration behaviors of the tested TBC samples can be explained as illustrated in Fig. 4(a), (b) and (c). In the case (a) with a low CMAS dosage, the molten CMAS is only dispersed locally due to lacking sufficient mass and or the surface wetting qualities. The low coverage reduces the number of CMAS infiltration possible start points through surface macro-sized defects (interconnected pores and open cracking). In case (b) with a medium dosage, the CMAS coverage is increased and there are more defective locations available for CMAS penetration. In case (c) with a high dosage, the coating surface should be fully covered by a layer of molten CMAS, and the chance for CMAS infiltration is maximized. Also, the CMAS layer can provide sufficient supply for continuous penetration from the coating surface to the inner coating, finally reach to the interface of topcoat and bondcoat.

The concentration of sand particles such as PM2.5 has been investigated in different environments. In the earth's atmosphere, relatively low levels of fine dust are ~5-35 µg/m^3 (Ref 17). However, some natural events such as volcanic eruptions and dust/sand storms led to elevated fine particulate levels as high as 13,000 µg/m^3 (Ref 18). Those dust particles ingestion into gas turbine engines can cause severe hot section components damage for both military and commercial aircraft operating. Now, the safe operating level for GTEs is presently set to $\leq$ 2000 µg/m^3 (Ref 19). In this study, the effect of CMAS dosage on the CMAS attack severity was confirmed, and the aggressive attack was confirmed at 35 mg/cm^2, therefore, this condition was used in follow-up CMAS exposure tests.

Effect of YAG Additive on CMAS Corrosion

The TBC samples #G1, 2, 3-5 were tested in air at 1250°C for 5 h with the CMAS dosage of about 35 mg/cm^2. The YAG addition to the low-k material was applied as the top layer of about 100-150 µm as shown in Fig. 2. The test was focused on the effect of the YAG additive in the TBC sample #G3-5 to improve CMAS resistance by comparing it with the TBC samples #G1-5 and G2-5. The top views of the morphologies of the tested TBC samples were observed under optical microscopes and are presented in Fig. 5.

All the tested samples were damaged by the CMAS attack to a different degree. The 8YSZ TBC sample #G1-5 appears to be the most damaged with large area spallation and mass loss, as well as deep penetration in the topcoat. Multi-layered delamination and separation are identified from the top viewed photo. In the low-k TBC sample #G2-5, the coating damage with large cracking is found and appears that CMAS penetration is limited to the near-surface region within the topcoat. However, there is spallation loss of the ceramic material in nearly half of the whole coating area. The YAG-modified TBC sample #G3-5 exhibits improved CMAS resistance by reducing the material loss and limiting the coating attack to some local areas. Instead of coating spallation, main coating failure occurred in the topcoat causing buckling of the material. The visual inspection of those TBC samples before and after cooling from 1250°C to room temperature, verified coating damages °Ccured during cooling time.

A distinct layer with a thickness of about 100 µm from the coating surface is identified. It is assumed that the layer is formed by CMAS infiltration in the layer, and the "dark grey" phase could be some new phase due to the reaction between the CMAS and the YAG composite material (Fig. 6). Based on the depth of the CMAS infiltration, it can be concluded that the addition of YAG to the low-k material matrix has inhibited the mobility of the CMAS attack frontier, and thus slows down the coating damage to some degree. This positive effect of YAG or similar additives to a TBC system had been investigated and confirmed by some researchers (Ref 20-22). Turcer et al. revealed that YAlO3 ceramic can be reacted with CMAS, and the reaction zone comprises three regions of reaction-crystallization products, including Y–Ca–Si apatite solid solution (*ss*) and $Y_3Al_5O_{12}$ (YAG)(*ss*).

In addition, the low-k TBC (#G2-5) demonstrated better CMAS resistance than the regular 8YSZ-TBC (#G1-5). This behavior can be explained by the co-doping of RE

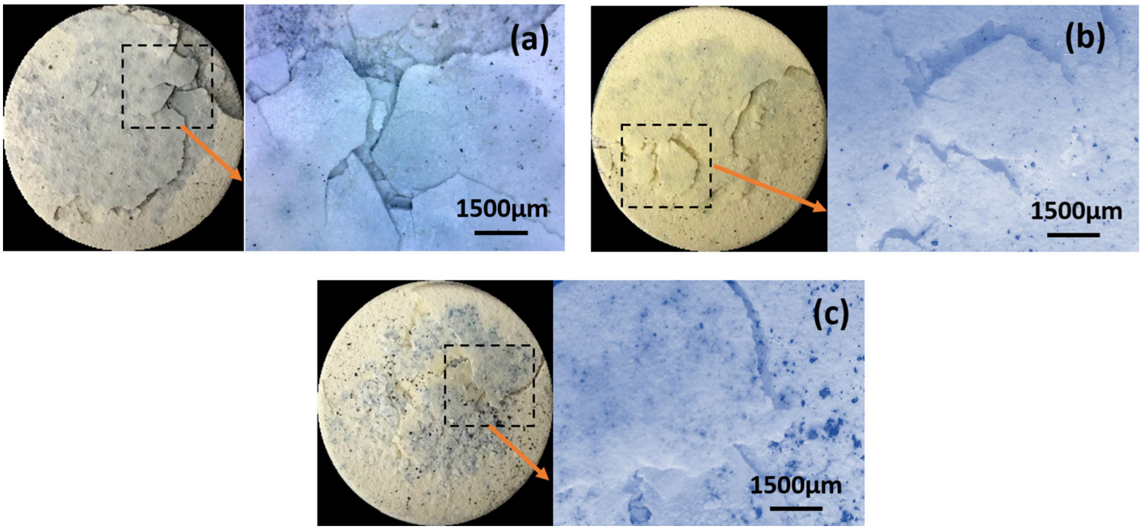

Fig. 5 Surface photographs of the TBC samples after the CMAS exposure test in air at 1250°C for 5 h. (a) TBC sample #G1-5: 8YSZ; (b) TBC sample #G2-5: Low-k; and (c) TBC sample #G3-5: YAG-modified low-k

oxides into ZrO_2. This formation of the disordered solid solution structure has lower diffusion coefficients and therefore suppressed reactivity with CMAS (Ref 23, 24).

XRD Analysis of the Reaction Between CMAS and YAG

To better understand the reaction between CMAS and YAG in the CMAS corrosion test, some test samples were manufactured and then tested by isothermal heat at 1250°C for 5 h. The test samples for the testing are shown in Table 3. Three TBC materials (G1, G2, G3) were well mixed with CMAS sand at a weight ratio of 1:1 (wt.%), then placed in a ceramic crucible separately prior to the reaction tests in air at 1250°C. For comparison purpose, a G3 powder sample and a G3 TBC sample were included in the XRD analyses.

The results of phase identification by XRD analyses are shown in Table 3. The results show that there is no major new phase formed in the sample #G1-S5 after the heating of the mixture of G1 (8YSZ) powder with CMAS sand for the duration of 5 h. Pujol et al. found that liquid-state CMAS will lead to the phase transition from stable t'-ZrO_2 to unstable m-ZrO_2 causing the change of volume of lattice, which can result in the failure of the 8YSZ-TBCs (Ref 25, 26). In the test sample #G1-S1, no m-ZrO_2 phase in the tested sample indicates that there is no major reaction between the G1 material and CMAS and no resultant phase transition. In addition, the CMAS with glassy structure (non-crystalline) is not detected in the XRD spectrum.

The reaction potential of the TBC materials #G2 and #G3 with CMAS was a main focus in the experiment. The XRD patterns for the test samples #G2-S5 and #G3-S5 are shown in Fig. 7 In the sample #G2-S5, a crystalline phase $Ca_2Mg[Si_2O_7]$ is identified in Fig. 7(a). Wu et al. investigated the CMAS corrosion behavior of the similar co-doped ZrO_2 TBC system at 1300°C, and found some new reaction phases such as $Zr_{84.4}Y_{5.6}Ta_{5.1}Ca_{4.9}$ were formed after reacting with CMAS for 50 h (Ref 27). In this test, no similar reaction products were detected in the XRD, possibly due to the difference in the test conditions (temperature, time, CMAS type,…). However, the formation of crystalline $Ca_2Mg[Si_2O_7]$ is beneficial for inhibiting CMAS mobility and attack severity based on Nitin et al. discovery in the TiO_2-Y_2O_3-ZrO_2 TBC system, where the TiO_2 promoted the formation of crystalline phase formation (Ref 8).

In the sample #G3-S5, a reaction product $NaO_{26}Si_6Y_9$ is confirmed in Fig. 7(b). XRD analysis was completed and determined the phase composition as: ZrO_2 phase at

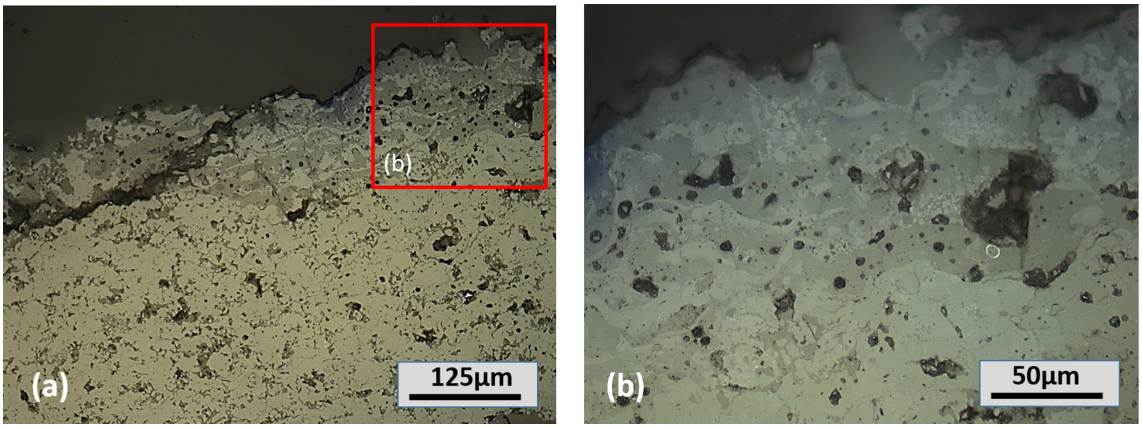

Fig. 6 Microstructures of the TBC sample #G3-5 with YAG additive in low-k material topcoat. (a) CMAS attacked coating near-surface area; (b) Close look on the attacked area

Table 3 List of test samples for CMAS reaction tests and XRD-phase analyses

Sample Code #	Test Sample Details and XRD Results	
	Chemical and Proc	XRD-Phase
G1-S5	G1 powder + CMAS	t' ZrO_2-Y_2O_3
G2-S5	G2 powder + CMAS	c + t' ZrO_2, $Ca_2Mg[Si_2O_7]$
G3-S5	G3 powder + CMAS	(c + t') ZrO_2, $Al_5O1_2Y_3$, $NaO_{26}Si_6Y_9$
G3-P1	G3 powder	c + t' ZrO_2, $Al_5O_{12}Y_3$
G3-C1	G3 coating, spray	c + t' ZrO_2, $Al_5O_{12}Y_3$

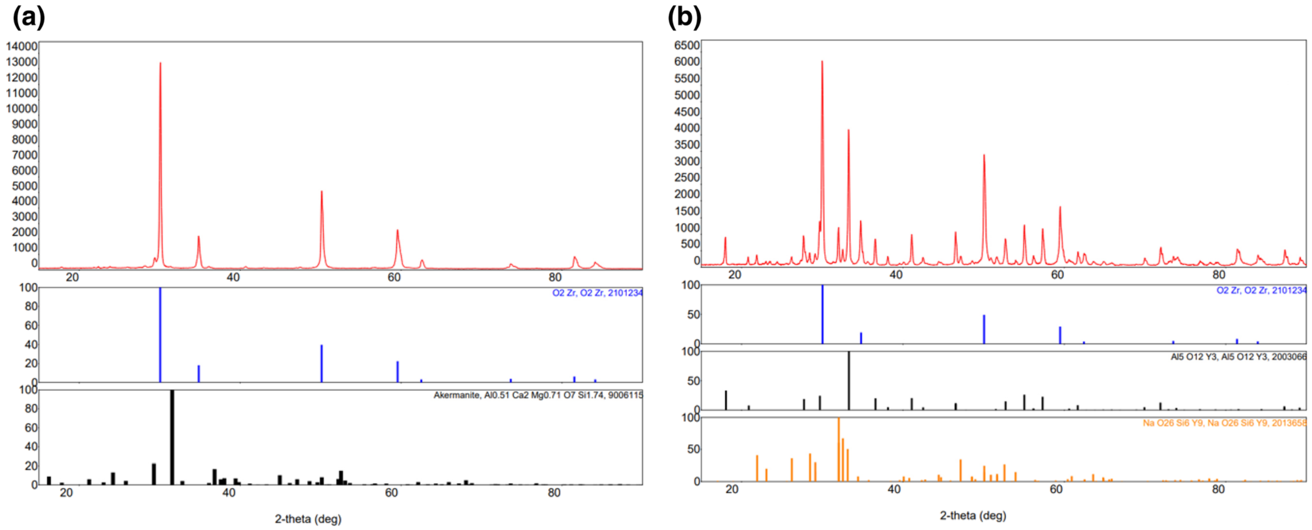

Fig. 7 XRD analyses of the ceramic materials mixed with CMAS sand after heated at 1250°C for 5 h. (a) Sample #G2-S5, (b) Sample #G3-S5

28.7 ± 0.4%, $Al_5O_{12}Y_3$ phase at 39.9 ± 0.6%, and $NaO_{26}Si_6Y_9$ phase at 31.4 ± 0.9%. The reaction product $NaO_{26}Si_6Y_9$ contains the elements Si, Na from the CMAS, and Y from YAG additive and or the co-doped low-k G2 material. It is clear that the CMAS is reactive to the YAG and or the RE oxide-doped TBC material. Based on the finding in the sample #G1-5, in which the CMAS has minor and slow reaction with the Y_2O_3-doped ZrO_2, it can be assumed that the major reaction occurred between the CMAS and the YAG ($Al_5O_{12}Y_3$) additive in the sample G3-S5. In addition, the large quantity of $NaO_{26}Si_6Y_9$ phase at 31.4 ± 0.9% indicated that the YAG additive is very reactive with the CMAS, and can result in quick reaction to transit liquid CMAS into crystalline solid product. This is expected to slow down the moving frontier of the CMAS infiltration in the TBC topcoat and sequentially inhibits the CMAS corrosion and TBC damage.

One of the methods for improving TBC CMAS resistance was modifying the TBC with the addition of active oxides or their compounds including RE oxides, TiO_2, and YAG. Godbole et al. found that the Y-containing system formed both garnet $A_2B_8(TO_4)_6O_2$ and apatite $A_3B_2T_3O_{12}$ (Ref 28, 29). $Y_3Al_5O_{12}$ (rare earth Y aluminate garnet, YAG) is stable in the CMAS-TBC system, and further can form more stable new reactant components. As a positive result, the formation of crystalline phases such as apatite and garnet has a two-fold effect on melt infiltration mitigation through a reduction in the melt volume and changes in the melt viscosity due to changes in the composition of the residual melt. Conclusively, our CMAS reaction tests are consistent with the previous related studies and confirm that the co-doped TBC (#G2) and the YAG-added TBC (#G3) can promote the formation of some crystalline products, and eventually change the properties of both CMAS and the phase components in the TBCs.

TBC Durability Test Under CMAS Attack

The long-exposure CMAS corrosion tests were conducted for TBC samples #G1, G2 and G3-120 at 1250°C for 120 h with a purpose to further investigate the degree of the CMAS attack and the failure mechanisms of the TBC samples with different chemical compositions. Firstly, it is confirmed that the CMAS attack becomes more severe and leads to more damage to those TBC samples with increased exposure times. Figure 8 shows the top surface views and the cross-section microstructures of the TBC samples after the 120-h CMAS corrosion test. Secondly, in the TBC sample #G1-120, the most severe CMAS attack on the 8YSZ topcoat was observed. The topcoat delaminated and spalled almost entirely at the bondcoat and topcoat interface. This indicates that the TBC had lost the protection of the topcoat. The TBC sample #G2-120 shows nearly full coverage of the ceramic coating. However, it is clear that the coating suffered multiple layered separation and partial spallation, thus leading to a lot of material loss. The coating damage occurred mostly within the low-k ceramic layer and at the 8YSZ layer and the low-k layer interface. Thirdly, the TBC sample #G3-120 exhibited the best CMAS attack resistance among the three TBC samples, though the CMAS attack and coating loss is still quite visible. A small area of the original coating surface is reserved with spallation, and the rest of the coating area is removed evenly, possibly indicating a more uniform CMAS attack in the coating region.

The microstructures of the tested TBC samples reveal the CMAS penetration into the coatings in different ways.

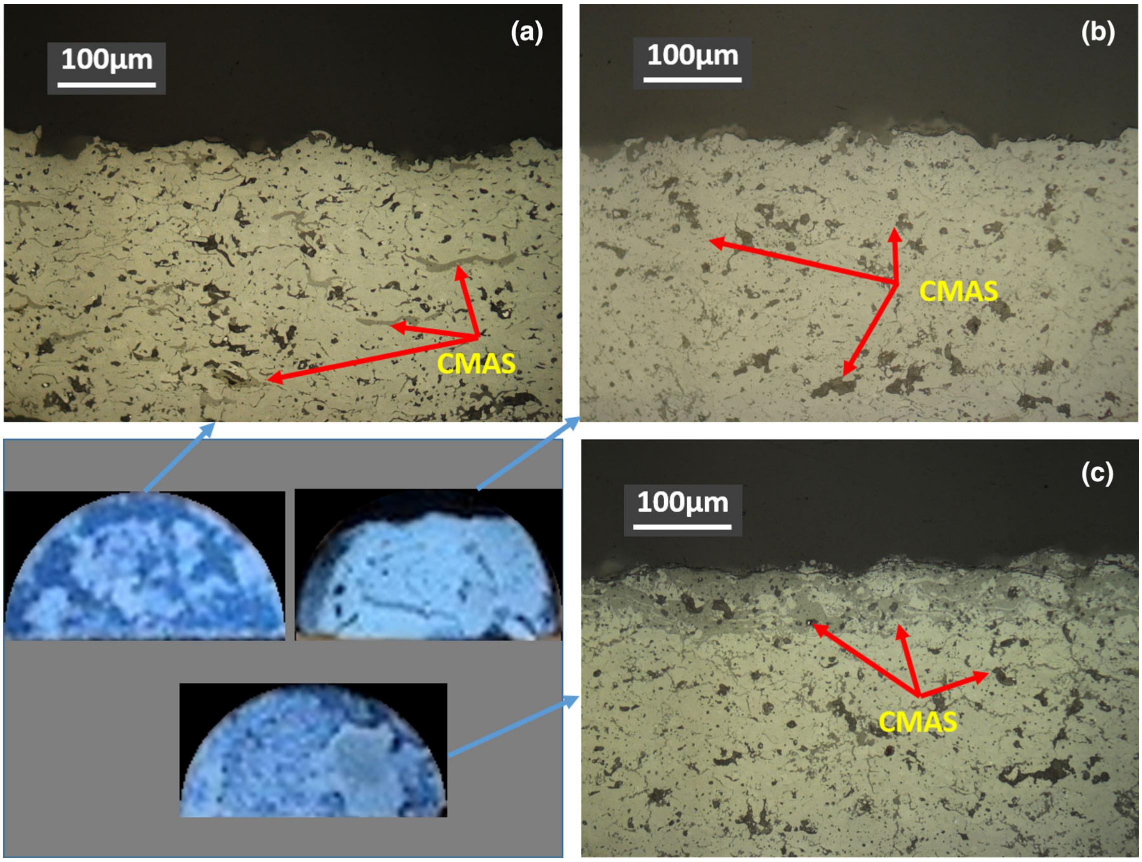

Fig. 8 Morphologies and microstructures of the TBC samples after CMAS corrosion tests at 1250°C for 120 h. (a) TBC sample #G1-120; (b) TBC sample #G2-120; (c) TBC sample #G3-120

In general, the liquid CMAS infiltrates and propagates from the TBC surfaces to the inner coatings predominantly through the coating defects mainly macro-porosity and cracks. In addition, the grain boundaries can also provide attack location as mentioned in some studies (Ref 30, 31), A YSZ-TBC could suffer grain-boundary corrosion by molten CMAS considerably due to the grain-boundary dissolution by molten CMAS, whereas high porosity and or fine crystalline grain structure leads to more severe TBC degradation. The TBC sample #G1-120 indicates CMAS infiltration through the coating defects and possible grain-boundary dissolution, whereas the distribution of both localized spots and horizontally lamellar CMAS is formed.

The TBC samples #G2-120 and #G3-120 show similar CMAS attack behaviors and no major lamellar reaction products are found in the coatings. However, a clear CMAS product is located within the top layer of the YAG-contained layer in sample #G3-120 in Fig. 8(c). Based on the results of the CMAS reaction tests, it is assumed that the CMAS reacted with the YAG additive and formed stable crystalline CMAS products, such as $NaO_{26}Si_6Y_9$, which enabled the inhibition of the CMAS mobility and reduced its reactivity with the TBC as well. Regarding the TBC sample #G2-120, it is believed that the improved CMAS resistance is attributed to the co-doped solute RE oxides in the low-k material. It is believed that this reduced the reaction between the molten CMAS and the TBC when compared with the 8YSZ-TBC sample #G1-120.

Analysis of SEM/EDXS in CMAS Attacked Coatings

The post examination on the tested TBC samples were performed using SEM/EDXS method as to provide more experimental evidences for determining CMAS penetration and attack mechanisms. The cross-sectional SEM photo micrograph and the corresponding elemental maps taken 10 µm below the surface (determined while carrying out SEM measurements) are shown in Fig. 9 for the sample #G3-5 of 5-h CMAS exposure; and in Fig. 10 for the sample #G3-120 of 120-h exposure.

There are three zones by color contracts identified in Fig. 9 i.e. (i) a dark grey zone within the top layer of the YAG-modified low-k TBC, (ii) a light grey zone, and (iii) light coating zone. The results of EDXS compositional analyses in the three zones are given in Table 4. In the dark zone (i), the rich elements are Al and Y from the YAG

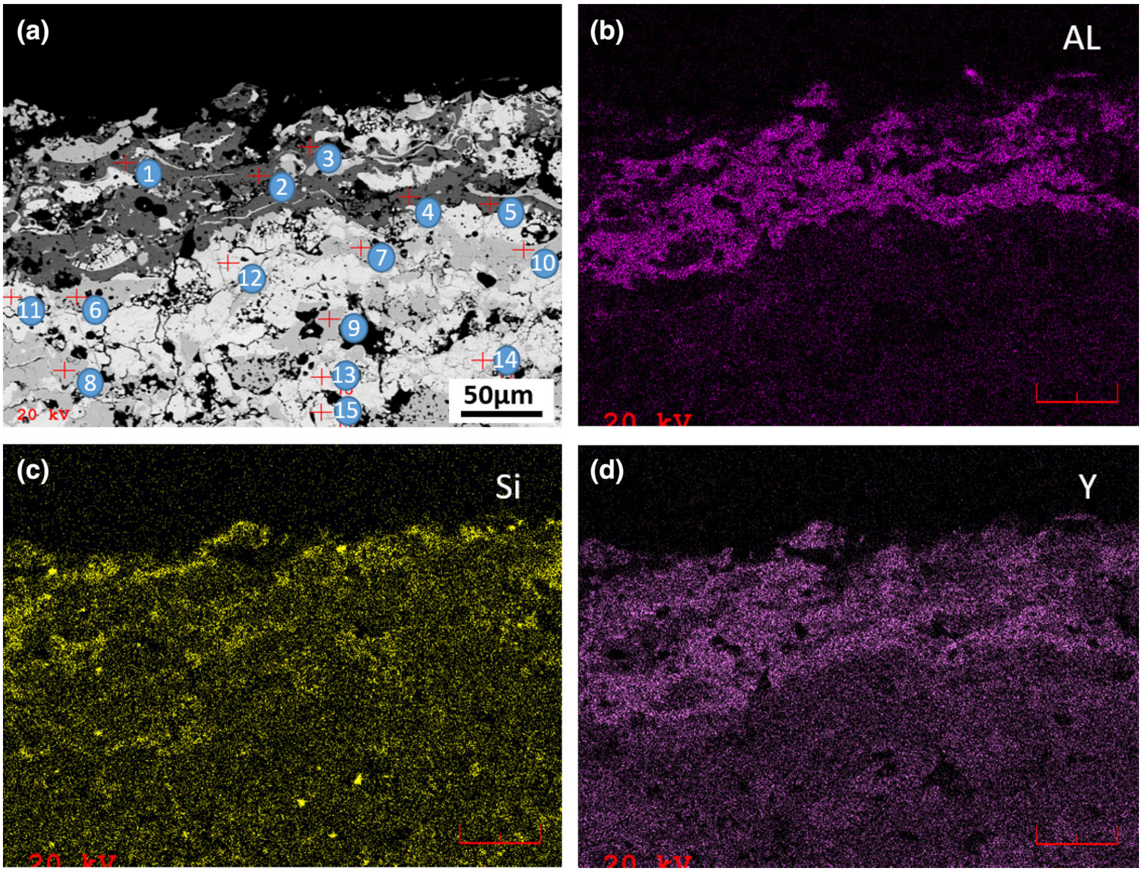

Fig. 9 Cross-sectional SEM micrograph and the corresponding EDXS element scan maps of the TBC sample #G3-5 after CMAS corrosion tests at 1250°C for 5 h. (a) BSE image, (b) map for element Al, (c) map for element Si, and (d) map for element Y

additive, as well as Ca, Si, and Mg from CMAS, indicating the dark phase will be YAG/CMAS mixture and or most likely their reaction product. In the light zone (ii), the rich element is Zr from the low-k ZrO_2 and the minor elements are Al from YAG and Ca from CMAS. Thus, the zone should locate in the main low-k TBC matrix, and consist of the main low-k TBC with a small amount of YAG/CMAS reaction product. In the light zone (iii), the rich elements are Zr, and the minor elements are Al, Y from YAG, and Ca, Si and Mg from CMAS. The elements maps of Si (shown in Fig. 9c) and Ca and Mg (scanned, but not shown) from CMAS, indicate that most of the CMAS is captured in the near-surface "dark" zone in the coating of the YAG + low-k layer, and a small amount of CMAS penetrates in the coating, at a depth of at least the view in Fig. 9. Conclusively, the CMAS attack is limited mainly in the near-surface region (i) about 100-150 µm corresponding to the top layer of YAG + low-k ZrO_2, whereas regions (ii) and (iii) are correlated to the unaffected, minor infiltrated or reacted CMAS that was able to infiltrate through the coating defects.

Similarly, three zones are identified in sample #G3-120 in Fig. 10. In addition, a dark surface layer above the coating is detected. The compositions of the three zones are quite comparable to those in sample #G3-5, indicating the CMAS attack process is the same as sample #G3-5. The dark surface layer is comprised of main CMAS elements and Al and Y from YAG, and thus provides evidence of the reaction of CMAS and YAG on the coating surface with the prolonged exposure time.

The reaction product should be $NaO_{26}Si_6Y_9$ (see Table 3) as revealed in the CMAS/TBC #G3-S5 reaction test by the XRD analyses. In Fig. 10, the coating separation takes place in the inner coating, corresponding to the severity of CMAS attack with increasing exposure time.

The beneficial effect of some additives, such as RE oxides and YAG, has been explained by optical basicity theory (Ref 32-34). Trucer et al. considered an initial screening criterion for choosing CMAS-resistant EBC ceramics. This criterion includes small optical basicity (OB or Λ) difference between CMAS and a given EBC ceramic. Based on this simple criterion, Si-free $YAlO_3$, γ-$Y_2Si_2O_7$, β-$Yb_2Si_2O_7$, and β-$Sc_2Si_2O_7$ have been identified as a

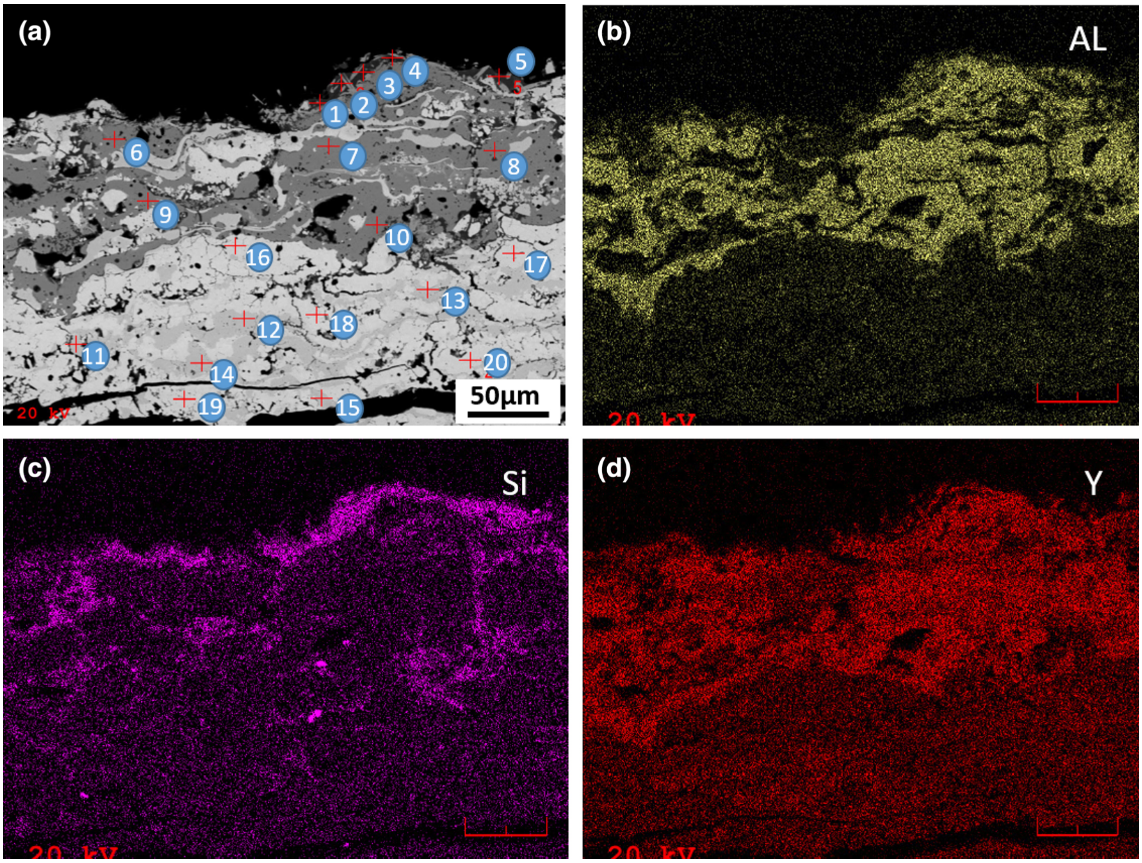

Fig. 10 Cross-sectional SEM micrograph and the corresponding EDXS element scan maps of the TBC sample #G3-120 after CMAS corrosion tests at 1250°C for 120 h. (a) BSE image, (b) map for element Al, (c) map for element Si, and (d) map for element Y

Table 4 Results of SEM/EDXS analyses in TBC samples #G3-5 and #G3-120 after the CMAS attack at 1250°C

Point#	Detection Zone/Area	Zr	Al	Ca	Y	Si	Mg	Na	RE
	1. TBC Sample G3-5 in Fig. 9: SEM/EDXS Result, % average								
P1-5	Dark gray affected zone	0	26.3	0.6	71.4	1.3	0.4		
P6-10	Light gray affected zone	99.3	0.4	0.3					
P11-15	Main coating zone	74.1	2.7	0.2	7.0	0.9	0.1	15	
	2. TBC Sample G3-120 in Fig. 10: SEM/EDXS Result, % average								
P1-5	Dark surface layer	0	28	20.4	7.8	42.3	0.3	1.1	
P6-10	Dark gray affected zone	0	26.6	0.9	70.9	1.5	0.6		
P11-15	Light gray affected zone	88.8	0.5	0	11.3				
P16-20	Main coating zone	69.7	0.1	0.2	6.4	0.5	0		23.0

promising CMAS-resistant EBC ceramics. CMAS typically has low optical basicity values, typically in the range of 0.55-0.65, rendering them basic oxides. In contrast, TBCs are typically greater than 0.8. Several investigations have shown that large differences in optical basicity ($\Delta\Lambda$) between CMAS former and TBC lead to more severe degradation and attack of the TBC. Kumar et al. showed that a YAG TBC ($\Lambda = 0.70$) has a lower $\Delta\Lambda$ with two types of CMAS used, as compared to a conventional YSZ TBC ($\Lambda = 0.87$). The reactivity and associated damage were lower for the YAG TBC (Ref 10). Another theory for the effect of reactive oxides in inhibiting CMAS attack is the promotion of the transition of CMAS into crystalline phases. Both the theories can be applied to the improvement for CMAS corrosion resistance in the co-doped low-k TBC samples (#G2) and the YAG-modified low-k TBC samples (#G3).

The influence of the CMAS composition on the formation of a reactive or protective layer can also play a key role in the TBC CMAS resistance or damage. As many studies indicated, specific CMAS chemistry of the CMAS deposits varied from type to type due to the variation in sand chemistry with difference sources and or locations, and even from location to location on the same blade surface (Ref 35). The CMAS used in this investigation mainly is made from quartz (34wt.%), gypsum (30%), aplite (17%), dolomite (14) and salt (5%). A variety of other CMAS chemistries are also reported: mono-, di- and tri-calcium silicates, spinel, anorthite ($CaAl_2Si_2O_8$), augite and melilite (Ref 35-37). In author's early work (Ref 8), CaO-Al_2O_3–SiO_2 (wt.%) ternary phase diagram shows a simulated CMAS glass composed of psuedowollastonite and anorthite fields, and other crystalline phases such as $CaAl_2Si_2O_8$ (Anorthite) and $Al_2Si_6O_{13}$ (Mullite). Solid solution of reactive oxides such as Al_2O_3 and TiO_2 into ZrO_2 (8YSZ) could serve as a nucleation agent to promote crystallization of the CMAS glass and sequentially result in the nearly complete crystallization of the leading edge of the CMAS front into anorthite, essentially arresting the front attack inward. Similarly, Si-free $YAlO_3$(YAP) EBC ceramic resulted in a CMAS reaction zone comprising three regions of reaction-crystallization products, including Y–Ca–Si apatite solid solution and $Y_3Al_5O_{12}$ (YAG) (Ref 20). Meanwhile, after γ-$Y_2Si_2O_7$ interaction with CMAS at 1500°C for 24 h, EDXS chemical analyses indicated the formation of different reaction products in term of the local CMAS chemistry, including the reaction products of Y–Ca–Si Apatite, Y–Ca–Si Apatite and CMAS glass. Though the CMAS reaction products could be very complex, but the test results revealed that the addition of reactive oxides can interact with some components in CMAS to form thermal stable phases and even a protective layer, and thus mitigate CMAS damage.

In summary, the phase composite low-k TBC demonstrated better CMAS corrosion resistance at the given test conditions when in comparison with regular 8YSZ-TBC. Further improvement can be achieved by the addition of YAG phase into the low-k TBC matrix. So far, the analytical data from the tested TBC samples revealed two possible mechanisms for inhibiting CMAS infiltration and mobility. These mechanisms include the formation of crystalline CMAS reaction products in the low-k TBC (#G2) and the formation of reaction products between CMAS and YAG and or RE oxides. The coating failure mechanisms were identified by molten CMAS penetration inward through the preferred paths of coating defects. These defects included macro-pores, open cracks and splat boundaries. Coating delamination and or spallation during cooling process led to the final coating failure, as shown in Fig. 4. Future tests focusing on the investigation of each stages of CMAS attack and propagation are expected to better control and inhibit coating degradation and damages.

Conclusion

This present work aimed to test and characterize the phase composite low-k TBC and the YAG-modified low-k TBC in different CMAS corrosion conditions in air at 1250°C. The behaviors of the TBCs under CMAS attack and coating failure mechanisms were investigated and discussed. The main results are summarized as:

- The CMAS dosage had a major effect on the severity of CMAS corrosion. The more CMAS dose applied to the TBC surfaces, the more damage in the TBC samples. The results could be explained by the CMAS wetted surface areas and the number of the defect sites for the CMAS attack initialization.
- The short-term CMAS exposure test revealed that the CMAS attack was very aggressive and caused coating damage in all the TBC samples. Relatively, the degradation of the low-k TBC and its YAG-modified TBC was inhibited to some degree. Especially, the YAG additive was more effective to slow down the process of CMAS infiltration.
- The long-term CMAS exposure caused much more serious coating damage and failure, indicating the penetration of CMAS toward the inner coating is a factor of time, if only the existence of the coating defects mainly including macro-porosity and cracking as well as grain and splat boundaries. However, the compositions of RE oxides and added YAG in the TBCs had played some key roles in inhibiting the CMAS infiltration.
- Based on the XRD and SEM/EDXS analyses, it was proven that the CMAS corrosion resistance of the composite phase TBC was improved by applying a YAG-contained top layer, wherein the YAG additive reacted with CMAS to transit liquid CMAS into crystalline CMAS (soluted) and reactant phases and thus reduced the CMAS mobility to penetrate deeply.
- All TBC samples failed during the cooling process from the test temperature to room temperature. Therefore, the coating failure mechanism can be attributed to the loss of the ceramic toughness and coating integrity due to the CMAS infiltration. The coating failure locations and modes are quite dependent on the coating material, structure, defect level, and exposure duration.

Acknowledgments The authors gratefully acknowledge technical assistance and experimental support from Mr. D. Reynolds and Ms. K. Rivellini, Curtiss-Wright, East Windsor, CT; and Ms. A. Stutzman for SEM/EDXS analyses at IMR Test Lab.

References

1. S. Kramer, J. Yang, C.G. Levi, and C.A. Johnson, Thermochemical Interaction of Thermal Barrier Coatings with Molten CaO-MgO-Al_2O_3-SiO_2 (CMAS) Deposits, *J. Am. Ceram. Soc.*, 2006, **9**(10), p 3167-3175.
2. C.G. Levi, J.W. Hutchinson, M. Vidal-Sétif, and C.A. Johnson, Environmental Degradation of Thermal Barrier Coatings by Molten Deposits, *MRS Bull*, 2012, **37**, p 932-941.
3. J. Kim, M.G. Dunn, A.J. Baran, D.P. Wade, and E.L. Tremba, Deposition of Volcanic Materials in the Hot Sections of Two Gas Turbine Engines, *J. Eng. Gas Turbines Power*, 1993, **115**(3), p 641-651.
4. D.R. Clarke, M. Oechsner, and N.P. Padture, Thermal-Barrier Coatings for More Efficient Gas-Turbine Engines, *MRS Bull.*, 2012, **37**(10), p 891-898.
5. D.J. DeWet, R. Taylor, and F.H. Stott, Corrosion Mechanisms of ZrO_2-Y_2O_3 Thermal Barrier Coatings in the Presence of Molten Middle-East Sand, *J. Phys. IV.*, 1993, **3**(C9), p 655-663.
6. M. Craig, N.L. Ndamka, R.G. Wellman, and J.R. Nicholls, CMAS Degradation of EB-PVD TBCs: The Effect of Basicity, *Surf. Coat. Technol.*, 2015, **270**, p 145-153.
7. D.J. DeWet, F.H. Stott, and R. Taylor, Surface Engineering Volume II: Engineering Applications, Edited by P.K. Datta and J.S. Gray, The Royal Society & Chemistry, Chambridge, (1992), p 210
8. A. Aygun, A.L. Vasiliev, N.P. Padture, and X. Ma, Novel Thermal Barrier Coatings that are Resistant to High-Temperature Attack by Glassy Deposits, *Acta. Mater.*, 2007, **55**(20), p 6734-6745.
9. R. Darolia, Thermal Barrier Coatings Technology: Critical Review, Progress Update, Remaining Challenges and Prospects, *Int. Mater. Rev.*, 2013, **58**, p 315-348.
10. R. Kumar, E. Jordan, M. Gell, J. Roth, C. Jiang, J. Wang, and S. Rommel, CMAS Behavior of Yttrium Aluminum Garnet (YAG) and Yttria-Stabilized Zirconia (YSZ) Thermal Barrier Coatings, *Surf. Coat. Technol.*, 2015, **327**, p 126-138.
11. S. Kramer, J. Yang, and C. Levi, Infiltration-Inhibiting Reaction of Gadolinium Zirconate Thermal Barrier Coatings with CMAS Melts, *Am. Ceramic Soc.*, 2008, **91**(2), p 576-583.
12. L. Li, N. Hitchman, and J. Knapp, Failure of Thermal Barrier Coatings Subjected to CMAS Attack, *J Therm. Spray Technol.*, 2010, **19**, p 148-155.
13. A.K. Rai, R.S. Bhattacharya, D.E. Wolfe, and T.J. Eden, CMAS-Resistant Thermal Barrier Coatings (TBC), *Appl. Ceram.*, 2010, **7**(5), p 662-674.
14. X. Ma, K. Rivellini, P. Ruggiero, and G. Wildridge, Toward Durable Thermal Barrier Coating with Composite Phases and Low Thermal Conductivity, *J. Therm. Spray Tech.*, 2020, **29**(3), p 423-432.
15. X. Ma, K. Rivellini, P. Ruggiero, and G. Wildridge, Evaluation and Characterization of a Durable Composite Phase Thermal Barrier Coating in Solid Particle Erosion and Burner Rig Tests, *J. Therm. Spray Tech.*, 2021, **30**, p 69-80.
16. J. Gu, B. Wei, A.F. Berendt, A. Ghoshal, M. Walock, R.F. Reidy, D. Berman, and S.M. Aouadi, A Comparative Study Of Calcium–Magnesium–Aluminum–Silicon Oxide Mitigation in Selected Self-healing Thermal Barrier Coating Ceramics, *J. Mater. Res.*, 2020, **220**, p 2311-2320.
17. A. Donkelaar, R.V. Martin, and M. Brauer et al., Global Estimates of Ambient Fine Particulate Matter Concentrations from Satellite-Based Aerosol Optical Depth: Development and Application, *Environ. Health Perspect.*, 2010, **118**, p 847-855.
18. T. Thorsteinsson, T. Johannsson, and A. Stohl et al., High Levels of Particulate Matter in Iceland Due to Direct Ash Emissions by the Eyjafjallajokull Eruption and Resuspension of Deposited Ash, *J. Geophys. Res. Solid Earth*, 2012, **117**, p B00C05.
19. U. Kueppers, C. Cimarelli, and K.-U. Hess et al., The Thermal Stability of Eyjafjallajokull Ash Versus Turbine Ingestion Sands, *J. Appl. Volcanol.*, 2014, **3**, p 4-15.
20. L.R. Turcer, A.R. Krause, H.F. Garces, L. Zhang, and N.P. Padture, Environmental-Barrier Coating Ceramics for Resistance Against Attack by Molten Calcia-Magnesia-Aluminosilicate (CMAS) Glass: Part I, $YAlO_3$ and γY_2Si_2O, *J. Euro. Ceram. Soc.*, 2018, **38**(11), p 3905-3913.
21. L. Wei, L. Guo, M. Li, and H. Guo, Calcium-Magnesium-Alumina-Silicate (CMAS) Resistant Ba_2REAlO_5 (RE = Yb, Er, Dy) Ceramics for Thermal Barrier Coatings, *J. Euro. Ceram. Soc.*, 2017, **37**(15), p 4991-5000.
22. S. Kramer, J. Yang, and C.G. Levi, Infiltration-Inhibiting Reaction of Gadolinium Zirconate Thermal Barrier Coatings with CMAS Melts, *J. Am. Ceram. Soc.*, 2008, **91**(2), p 576-583.
23. D. Zhu and R.A. Miller, Development of Advanced Low Conductivity Thermal Barrier Coatings, *Int. J. Appl. Ceram. Technol.*, 2004, **1**, p 86-94.
24. X. Ma et al., Low Thermal Conductivity Thermal Barrier Coating Deposited by the Solution Plasma Spray Process, *Surf. Coat. Technol.*, 2006, **201**(7), p 4447-4452.
25. G. Pujol, F. Ansart, J.P. Bonino, A. Malié, and S. Hamadi, Step-by-Step Investigation of Degradation Mechanisms Induced by CMAS Attack on YSZ Materials for TBC Applications, *Surf. Coat. Technol.*, 2013, **235**, p 165-173.
26. M.H. Vidal-Sétif, C. Rio, D. Boivin, and O. Lavigne, Microstructural Characterization of the Interaction Between 8YPSZ (EB-PVD) Thermal Barrier Coatings and a Synthetic CAS, *Surf. Coat. Technol.*, 2014, **239**, p 41-48.
27. D. Wu, Y. Yao, X. Shan, F. Yang, X. Zhao, and P. Xiao, Equimolar $YO_{1.5}$ and $TaO_{2.5}$ Co-doped ZrO_2 as a Potential CMAS-Resistant Material for Thermal Barrier Coatings, *J. Am. Ceram. Soc.*, 2021, **104**(2), p 1132-1145.
28. E. Godbole, A. Handt, and D. Poerschke, Apatite and Garnet Stability in the Al–Ca–Mg–Si–(Gd/Y/Yb)–O Systems and Implications for T/EBC: CMAS Reactions, *J. Am. Ceram. Soc.*, 2022, **105**, p 1596-1609.
29. E. Godbole, N. Karthikeyan, and D. Poerschk, Garnet Stability in the Al–Ca–Mg–Si–Y–O System with Implications for Reactions Between TBCs, EBCs, and Silicate Deposits, *J. Am. Ceram. Soc.*, 2020, **103**, p 5270-5282.
30. S. Morell, V. Testa, G. Bolelli et al., CMAS Corrosion of YSZ Thermal Barrier Coatings Obtained by Different Thermal Spray Processes, *J. Euro. Ceram. Soc.*, 2020, **40**(12), p 4084-4100.
31. Z. Cai, J. Jiang, W. Wang, Y. Liu, and Z. Cao, CMAS Penetration-Induced Cracking Behavior in the Ceramic Top Coat of APS TBCs, *Ceram. Intl.*, 2019, **45**(11), p 14366-14375.
32. L.R. Turcer, A.R. Krause, H.F. Garces, L. Zhang and N.P. Padture, Environmental-Barrier Coating Ceramics for Resistance Against Attack by Molten Calcia-Magnesia-Alumino Silicate (CMAS) Glass: Part II, β-$Yb_2Si_2O_7$ and β-$Sc_2Si_2O_7$, *J. Eur. Ceram. Soc.*, 2018, **38**(11), p 3914-3924.
33. V. Dimitrov and S. Sakka, Electronic Oxide Polarizability and Optical Basicity of Simple Oxides, *J. Appl. Phys.*, 1996, **79**, p 1736-1740.
34. N.L. Ndamka, R.G. Wellman, and J.R. Nicholls, The Degradation of Thermal Barrier Coatings by Molten Deposits: Introducing the Concept of Basicity, *Mater. High Temp.*, 2016, **33**(1), p 44-50.
35. M.H. Vidal-Setif, N. Chellah, C. Rio et al., Calciummagnesium-Alumino-Silicate (CMAS) Degradation of EB-PVD Thermal Barrier Coatings: Characterization of CMAS Damage on Ex-service High Pressure Blade TBCs, *Surf. Coat. Technol.*, 2012, **208**, p 39-45.

36. M.P. Borom, C.A. Johnson, and L.A. Peluso, Role of Environmental Deposits and Operating Surface Temperature in Spallation of Air Plasma Sprayed Thermal Barrier Coatings, *Surf. Coat. Technol.*, 1996, **86-87**, p 116-126.
37. G. Witz, V. Shklover, W. Steurer et al., High-Temperature Interaction of Yttria Stabilized Zirconia Coatings with CaO-MgO-Al_2O_3-SiO_2 (CMAS) Deposits, *Surf. Coat. Technol.*, 2015, **265**, p 244-249.